

Aerodynamic Modeling of Propeller Forces and Moments at High Angle of Incidence

Yuchen Leng ^{*} Heesik Yoo [†] Thierry Jardin [‡] Murat Bronz [§]
and Jean-Marc Moschetta [¶]

ISAE-SUPAERO, Université de Toulouse, France

ENAC, Toulouse, France

A reduced-order model to estimate the aerodynamic forces and moments of a propeller at incidence angle from 0° to 90° was presented. The objective was to provide an inexpensive and effective approach to analyse propeller performance of a vertical/short take-off and landing (V/STOL) aerial vehicle during transition flight. The model was based on Blade Element Theory (BET) and was coupled with an extended momentum theory or Pitt & Peters inflow model to include the asymmetrical flow condition. The aerofoil aerodynamic data was provided by an empirical model that extended lift and drag polar to a broad angle-of-attack range suitable in transition flight. Furthermore a rotational stall delay model and a radial flow correction model have been incorporated to include primary 3-dimensional effects. The result has been presented and validated with past experiment and Unsteady Reynolds-Averaged Navier-Stokes (URANS) solution under similar conditions.

I. Introduction

In recent years, interest on Vertical Take-Off and Landing (VTOL) aerial vehicles has increased significantly. One promising configuration is the tilt-body/rotor aircraft. They orient their propellers in the vertical direction during take-off and landing like a conventional helicopter. The aircraft then enter a transition phase, where their body or rotors are rotated to align with a near horizontal flight direction for efficient wing-borne cruise. Concepts in different scales have been investigated in past studies from micro aerial vehicles like the tilt-body MAVION developed at ISAE-SUPAERO (Fig. 1a), to full-scale aircraft such as the tilt-rotor V-22 Osprey (Fig. 1b). During the transition from near-hover to horizontal cruise condition, flight parameters such as angle of attack, airspeed vary drastically¹ compared to a conventional aeroplane, and the airflow can no longer be assumed axisymmetric at the propeller disk.

A. Background

Previous studies have shown that a propeller at non-zero incidence angle α_p , which is measured between the rotation axis and free stream direction, is subjected to asymmetrical forces and moments in the propeller plane.³⁻⁵ Those aerodynamic efforts need to be taken into consideration for the design of flight control surfaces and transition flight control law. These decisions are relevant to aircraft configuration, and thus must be considered during preliminary design phase. For such purpose, a reduced-order model is desired to predict propeller performance at high incidence angle with affordable cost and reasonable accuracy.

Ribner studied the non-axial flight condition on airplane propellers.⁴ He modeled the propeller as a vertical fin that deflects the momentum to produce asymmetric load. Charts and formulae were presented to

^{*}Ph.D. Candidate at ISAE/DAEP, and Research Engineer at DELAIR, 10 Avenue Edouard Belin, Toulouse, France

[†]Advanced Master, Département d'Aérodynamique, Energétique et Propulsion, Institut Supérieur de l'Aéronautique et de l'Espace, 10 Avenue Edouard Belin, Toulouse, France

[‡]Research Scientist, Département d'Aérodynamique, Energétique et Propulsion, Institut Supérieur de l'Aéronautique et de l'Espace, 10 Avenue Edouard Belin, Toulouse, France

[§]Assistant Professor, UAV Lab, École Nationale de l'Aviation Civile, 7 Avenue Edouard Belin, Toulouse, France

[¶]Professor, ISAE, Département d'Aérodynamique, Energétique et Propulsion, Institut Supérieur de l'Aéronautique et de l'Espace, 10 Avenue Edouard Belin, Toulouse, France

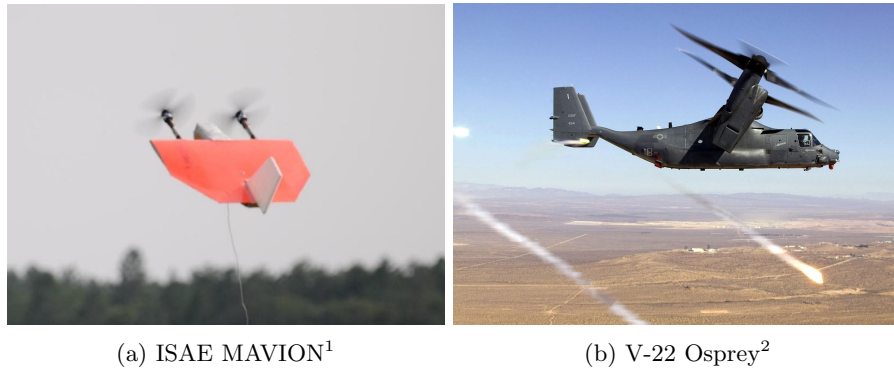


Figure 1: VTOL aircraft concepts

predict the thrust and moment gradient at small incidence angle taking into account the propeller geometry. Those results were later simplified and extended towards moderate incidence angle by de Young.⁵

Ribner's model assumes uniform load distribution across the propeller blade, and thus can't produce load distribution and accuracy decreases at high incidence or low blade number.

Meanwhile Blade Element Momentum Theory (BEMT) has proven to be an effective tool for propeller and wind turbine analysis. There is several work done to extend BEMT for non-axial flight. Crigler⁶ proposed such a BEMT model for aircraft propellers. The local flow condition at each blade section has been assumed to be uniform across the annular ring during the solution process of the respective blade section. The method calculates radial varying blade loading and shows non-uniform loads on the propeller disk. However, the validity of extending local flow condition to full annulus is not justified.

Based on the previous work in modeling non-axial flight using BEMT, Smith⁷ has presented a non-uniform BEMT method by dividing a propeller annulus into segments, each segment corresponds to a different propeller blade. Flow condition is only assumed to be uniform within one annulus segment. The segmented BEMT, although produces velocity discontinuities at annulus edge, better captures the azimuthally dependent load variation. But his implementation still suffers numerical stability issue and may be improved to include the stall delay phenomenon at low advance ratio.

However the validity of BEMT at high incidence angle hasn't been justified. Bramwell⁸ pointed out that the differential form of momentum equation is a special case in axial flight. When at incidence, or forward flight condition for helicopter rotor, the pressure field satisfies Laplace equation under small perturbation assumption, and thus the velocity field at propeller disk must be obtained as integral of pressure gradient instead of merely from local blade section load. The theory leads to the development of various inflow model.^{9,10} The pressure distribution along the disk is represented by a series expansion of Legendre polynomials, and induced velocity field is calculated through analysis of its integral form. These models have been widely applied in predicting helicopter performance at high forward speed condition^{11,12} and wind turbines in yaw.¹³

In the scope of a reduced-order model for preliminary proprotor analysis, both BEMT and inflow methods show promising aspects but also have their drawbacks. Although BEMT is good at capturing radial induced velocity distribution, it is unable to predict the longitudinal induced velocity variation due to incorrectly assuming local association between induced velocity and blade load. Thus BEMT is not able to predict a pitch moment originated from the upwash at rotor disk leading edge. On the other hand, inflow model doesn't hold such an assumption, but its lower-order implementation assumes induced velocity to be small disturbance compared to free stream in order to linearise the Euler's equations, and thus is slow to converge at low advance ratio.

B. Present work

The current study aims at creating a rapid analysis tool to predict propeller forces and moments at incidence angle range between 0° and 90° , from near-hover to high-speed flight. The tool was developed from ISAE MAVLab, which is a BEM method programmed in MATLAB. The program was extended to allow azimuthal blade load variation. For high advance ratios, inflow method was used instead of BEM to better predict

in-plane forces and moments. Furthermore, aerodynamic effects for propeller at high incidence have been identified and modeled through comparison with experimental data.

Experimental data has been extracted from full-scale wind tunnel test conducted by Yaggy et al.¹⁴ The 12-foot-diameter propeller was mounted in the Ames 40- by 80-foot wind tunnel and could be rotated from 0° to 85° incidence angle. The blade pitch angle could be changed but the current study focuses on the comparison with 35° pitch angle case, which is measured at 75% radius.

The paper is organised as follows. In Section II, the theoretical basis of the reduced-order model is introduced. The extended BEMT method and Pitt & Peters inflow model are presented, along with two additional aerodynamic models to correct 2D lift and drag coefficients for the 3D effects on propeller blade. The flow component along the radial direction is associated with delayed stall on the blade section and additional drag along the radial direction, and thus have to be modelled for accurate prediction on aerodynamic forces and moments. In Section III theoretical result is validated by experimental data and solution from Unsteady Reynolds-Averaged Navier-Stokes (URANS) equations.

II. Model Description

The aerodynamic loads on the propeller is calculated through Blade Element Theory (BET) coupled with either momentum theory or inflow model. In BET, to determine the angle of attack on the blade element, the induced velocity must be included. For small advance ratio, its value is determined by an extended momentum method based on the implementation of Winarto.¹⁵ This approach is presented in section C, it reduces the equations into a single-variable root finding problem such that numerical stability is improved¹⁶ for cases with high incidence. For higher advance ratio ($J \geq 0.3$), Pitt and Peters inflow model⁹ is used to calculate induced velocity distribution across rotor disk. The method is well documented, and thus will only be briefly discussed in section D.

A. Definition of Propeller Coordinate

To properly describe propeller loads, it is necessary to define a coordinate system fixed with the hub. In this study the free propeller is subjected to a free stream velocity U_∞ not aligned with its axis of rotation X_p , as shown in figure 2. The angle between axis of rotation and free stream velocity is defined as the incidence angle α_p . It is limited between 0° and 90° in current study, beyond which empirical models should be used to solve induced velocity and blade loading.⁸

The propeller coordinate system is centred at the rotor disk centre, and is defined by the rotor orientation relative to free stream velocity. X_p axis is perpendicular to the propeller disk and points forward. Z_p axis is defined in the propeller plane, and points in the opposite direction as the in-plane component of free stream velocity $U_Z = U_\infty \sin \alpha_p$. And Y_p axis is defined by right-hand law. A standard propeller rotates with angular velocity Ω in the positive X_p direction.

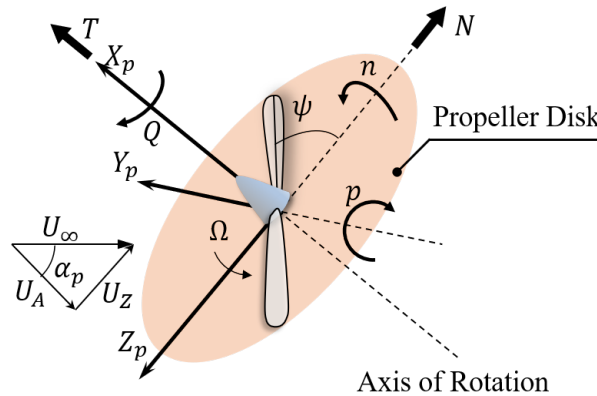


Figure 2: Definition of Propeller Coordinates

Current study focuses on two forces and two moments acting on the propeller: thrust T , torque Q , normal force N and yaw moment n , which are also shown in figure 2. Thrust T is defined to be the force component in the positive X_p direction. Torque Q is the moment component in the X_p axis and is positive

when acting against rotation. Normal force N is in the same direction as U_Z , and yaw moment n is in positive Z_p direction.

Those forces and moments are not steady but changes when propeller rotates. The azimuthal position of the blade is described by the angle ψ , where a superscript j may be added to indicate a specific blade number. The angle ψ is defined to be zero when the blade radius lies on positive Z_p axis. ψ increases for a rotation in X_p direction. Following the conventions, propeller blades at azimuthal position $0 < \psi < \pi$ “advance” into the free stream flow, and thus this side of propeller disk is referred to as the “advancing side”. Similarly, the side where $\pi < \psi < 2\pi$ is referred to as the “retreating” side, as blades “retreat” away from the free stream wind.

B. Blade Element Analysis

The blade element analysis is similar to conventional BET, but needs to take in-plane component from free stream velocity into account. As illustrated in figure 2, a free stream component $U_Z = U_\infty \sin \alpha_p$ is in the propeller coordinate Z_p direction. This component appears because the free stream velocity comes at incidence angle α_p , and its existence makes the flow condition no longer axisymmetric but change with azimuthal position ψ .

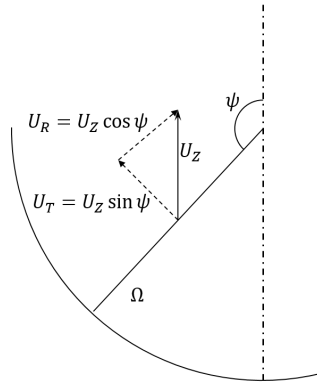


Figure 3: Decomposition of In-Plane Velocity V_Z

Seen from the front, at an arbitrary azimuthal position ψ , the in-plane component U_Z can be further decomposed at the propeller blade into two components: U_T in the tangential direction and U_R in the radial direction. According to figure 3, the two components are decomposed as follows.

$$U_T = U_Z \sin \psi = U_\infty \sin \alpha_p \sin \psi \quad (1)$$

$$U_R = U_Z \cos \psi = U_\infty \sin \alpha_p \cos \psi \quad (2)$$

The radial component U_R is important in drag estimation along the blade span-wise direction, hence the normal force prediction. It doesn't directly affect axial and tangential forces, and thus will be ignored in the derivation of BET method. The correction on normal force prediction is presented in section E. The tangential component U_T is in the blade section plane, and consequently its contribution is included in blade element analysis.

The flow velocities for an advancing side blade section are schematically shown in figure 4.

The relative wind velocity W is composed of three different parts: 1. rotational velocity Ωr ; 2. free stream velocity in the blade section U_∞^ψ ; and 3. induced velocity V^ψ . The superscript $^\psi$ means variables are dependent on azimuthal position ψ . The projection of free stream velocity in blade section plane U_∞^ψ contains the in-plane velocity in the blade tangential direction, and therefore changes the relative wind magnitude W and its angle of attack α .

Note that, in the diagram, induced velocity contains both axial and tangential components: V_A^ψ is the axial induced velocity and V_T^ψ is tangential swirl velocity. They are determined by either momentum method or inflow model introduced later.

The sectional lift and drag is given by 2D aerofoil aerodynamics.

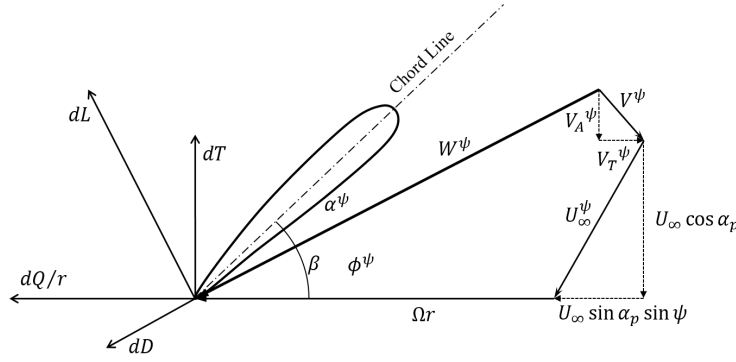


Figure 4: Velocity Diagram for Advancing Blade Section

$$dL = \frac{1}{2} \rho W^2 C_L c dr \quad (3)$$

$$dD = \frac{1}{2} \rho W^2 C_D c dr \quad (4)$$

where C_L and C_D are 2D lift and drag coefficients as functions of sectional Reynolds number Re , Mach number M and angle of attack α . c is the local chord length, and dr is differential radius.

Angle of attack α can be found as the difference between blade pitch angle β and inflow angle ϕ of the relative wind velocity. For propeller at incidence, the angle-of-attack range can be broad, and thus require special models to generate post-stall aerofoil behaviour, such treatment is not the focus of current study. An empirical model has been developed based on Bianchini et al.¹⁷ For this reason, the functional relations of C_L and C_D are assumed to be known.

The resultant sectional lift and drag are converted into differential thrust and tangential force through the inflow angle ϕ . The usual small angle approximation of ϕ is not employed due to possible large variation of ϕ at high incident angle.

$$dT = \frac{1}{2} \rho W^2 c (C_L \cos \phi - C_D \sin \phi) dr \quad (5)$$

$$dQ/r = \frac{1}{2} \rho W^2 c (C_L \sin \phi + C_D \cos \phi) dr \quad (6)$$

To obtain overall thrust, torque among other forces and moments, the results need to be integrated along the blade and then averaged in one period. Averaging is necessary since the propeller loading is dependent on azimuthal position, and aircraft dynamic concerns mostly overall propeller performance.³

$$\begin{aligned} T &= \frac{1}{2\pi} \int_0^{2\pi} \int_0^R \left(\frac{dT}{dr} \right) dr d\psi & N &= \frac{1}{2\pi} \int_0^{2\pi} \int_0^R \left(\frac{dQ/r}{dr} \sin \psi \right) dr d\psi \\ Q &= \frac{1}{2\pi} \int_0^{2\pi} \int_0^R \left(\frac{dQ/r}{dr} r \right) dr d\psi & n &= -\frac{1}{2\pi} \int_0^{2\pi} \int_0^R \left(\frac{dT}{dr} r \sin \psi \right) dr d\psi \end{aligned} \quad (7)$$

Though the flow is not axisymmetric, the propeller loading is nevertheless periodic.¹⁸ Therefore it is not necessary to average the propeller through a complete rotation. The forces and moments only need to be averaged for one loading period, which equals to $\frac{2\pi}{B\Omega}$ (B is blade number), and then the result can be obtained by summing up components from all propeller blades.

$$\begin{aligned} T &= \sum_{j=1}^B \frac{B}{2\pi} \int_{(j-1)\frac{2\pi}{B}}^{j\frac{2\pi}{B}} \int_0^R \left(\frac{dT}{dr} \right) dr d\psi & N &= \sum_{j=1}^B \frac{B}{2\pi} \int_{(j-1)\frac{2\pi}{B}}^{j\frac{2\pi}{B}} \int_0^R \left(\frac{dQ/r}{dr} \sin \psi \right) dr d\psi \\ Q &= \sum_{j=1}^B \frac{B}{2\pi} \int_{(j-1)\frac{2\pi}{B}}^{j\frac{2\pi}{B}} \int_0^R \left(\frac{dQ/r}{dr} r \right) dr d\psi & n &= -\sum_{j=1}^B \frac{B}{2\pi} \int_{(j-1)\frac{2\pi}{B}}^{j\frac{2\pi}{B}} \int_0^R \left(\frac{dT}{dr} r \sin \psi \right) dr d\psi \end{aligned} \quad (8)$$

C. Momentum Analysis

Previous paragraphs detailed a method to resolve blade section force from local flow condition and aerofoil aerodynamic data. This requires the induced velocity V^ψ to be known. In part 1 the equations that associates induced velocity with sectional loading will be established using momentum balance. Those equations generally don't have closed-form solutions, and the solution technique will be presented in part 2.

1. Momentum equations

In conventional BEM theory, the momentum analysis is performed upon a stream tube that passes an annulus at given radius r and has a differential width dr , as illustrated in figure 5a and 5b.

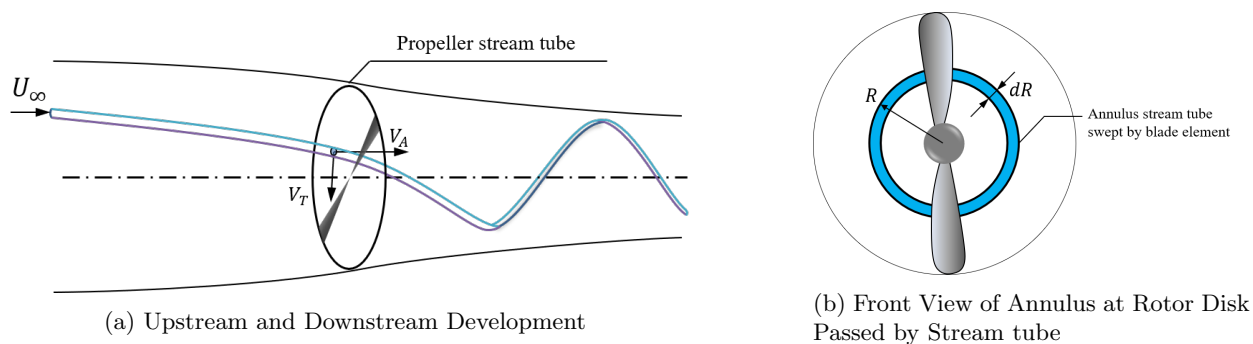


Figure 5: Stream tube Passing through Propeller Disk

The fluid far upstream in this stream tube is assumed to be at ambient condition. The flow is incompressible.

Across the rotor disk, the flow velocity stays continuous and a uniform static pressure jump is added to simulate the propeller loading. Through momentum conservation, the fluid accelerates as it approaches the rotor disk, and will continue accelerating to a finite velocity far downstream, resulting in a contracting stream tube seen in figure 5a. Theoretical derivation shows that the induced velocity at the rotor disk is a half of the ultimate velocity increase.¹⁹

To admit non-uniform flow condition over the annulus, each of them is further divided into equally distributed arc segments by the number of blade.⁷ For example, the annulus for a 2-blade propeller is separated into 2 arc segments of 180° as shown in figure 6, with only axial induced velocity shown for clarity. The associated propeller blade and annular flux are coloured the same. Superscripts indicate different blades.

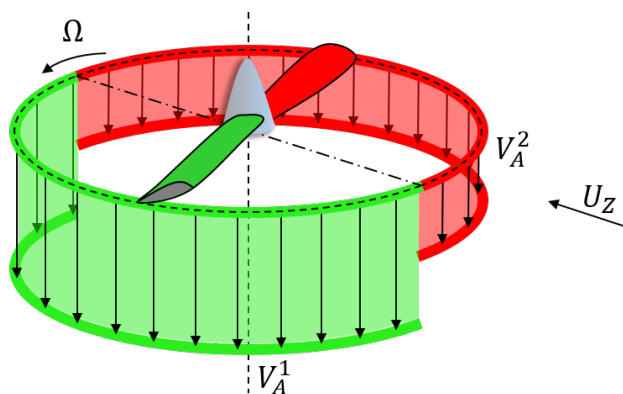


Figure 6: Segments for Rotor Disk Annulus of a 2-Blade Propeller

Each blade section is associated with the arc segment that contains it. When performing blade element analysis, the induced velocity will be taken as the average value over the associated arc. Each segment will be analysed independently.

Consider arc segment at position r and the associated blade j , the incremental thrust across the arc segment can be found

$$dT^j = \int_{\psi_{0j}}^{2\pi/B} 2\rho \left(U_A + V_A^j \right) V_A^j r d\psi dr \quad (9)$$

Recall that induced velocity is considered as an average value across arc segment, and thus the integrand in ψ is a constant function.

$$dT^j = \frac{4\pi}{B} \rho \left(U_A + V_A^j \right) V_A^j r dr \quad (10)$$

which is the incremental thrust generated by induced momentum flux over this arc segment.

Similar analysis yields the tangential force expressed as angular momentum change due to swirl velocity.

$$dQ^j/r = \frac{4\pi r}{B} \rho \left(U_A + V_A^j \right) V_T^j r dr \quad (11)$$

The thrust and torque obtained should be the same as found in blade element analysis in section B. Thus when the left-hand-side terms in equation 10 and 11 are substituted using their counterparts in BET, the association between induced velocity and blade loading can be established in the form of BEMT.

2. Inflow angle equation

To solve both components of induced velocity V^ψ and hence ultimately blade loading, the momentum flux is balanced by the blade sectional force. From equation 5

$$dT^j = \frac{1}{2} \rho W^{j2} c \left(C_L^j \cos \phi^j - C_D^j \sin \phi^j \right) dr \quad (12)$$

Substitute into equation 10

$$\begin{aligned} \frac{4\pi}{B} \rho \left(U_A + V_A^j \right) V_A^j r dr &= \frac{1}{2} \rho W^{j2} c \left(C_L^j \cos \phi^j - C_D^j \sin \phi^j \right) dr \\ W^j V_A^j \sin \phi^j &= \frac{\sigma}{4} W^{j2} \left(C_L^j \cos \phi^j - C_D^j \sin \phi^j \right) \\ \frac{V_A^j}{W^j} &= \frac{\sigma}{4} \left(C_L^j \cos \phi^j - C_D^j \sin \phi^j \right) \csc \phi^j \end{aligned} \quad (13)$$

Notice that the right-hand-side terms is a function explicitly only in ϕ^j and $\sigma = \frac{Bc}{2\pi r}$ is local solidity. Aerodynamic coefficients are functions of angle of attack, Reynolds number and Mach number. The latter two are also function of relative wind W , but, in most cases, a weaker function. To include the influence of W , it is convenient to construct an inner iteration on ψ and an outer loop on W .

Similarly the tangential swirl velocity ratio can be expressed as another function in ϕ^j .

$$\frac{V_T^j}{W^j} = \frac{\sigma}{4} \left(C_L^j \sin \phi^j + C_D^j \cos \phi^j \right) \csc \phi^j \quad (14)$$

In order to solve the induced velocity, equation 13 and 14 should be coupled. Recall from the vector summation of relative wind velocity W^j .

$$\begin{aligned} U_A &= W^j \sin \phi^j - V_A^j \\ \frac{U_A}{W^j} &= \sin \phi^j - \frac{V_A^j}{W^j} \\ \frac{U_A}{W^j} &= \sin \phi^j - \frac{\sigma}{4} \left(C_L^j \cos \phi^j - C_D^j \sin \phi^j \right) \csc \phi^j = G(\phi^j) \end{aligned} \quad (15)$$

Similarly,

$$\frac{\Omega r + U_T}{W^j} = \cos \phi^j + \frac{\sigma}{4} \left(C_L^j \sin \phi^j + C_D^j \cos \phi^j \right) \csc \phi^j = H(\phi^j) \quad (16)$$

For simplicity, let $U_T' = \Omega r + U_T$. Apparently, relative wind velocity W^j should be identical in both equation, and thus

$$U_T' G(\phi^j) - U_A H(\phi^j) = 0 \quad (17)$$

To eliminate the singularity at $\phi^j = 0$, multiply both sides by $\sin \phi^j$ and the result gives a root-finding problem only in inflow angle ϕ^j .

$$[U_T' G(\phi^j) - V_X H(\phi^j)] \sin \phi^j = I(\phi^j) = 0 \quad (18)$$

The inflow angle equation 18 can be solved by various root-finding methods. Bisection method is used in the current study for stability concern. Once inflow angle ϕ^j is found, the induced velocity can be recovered from equation 13 and 14, hence the aerodynamic load on j -th blade element. The algorithm to solve one propeller section is schematically described in figure 7. The maximum number of iterations Itr_{max} is determined so that the bracketing interval becomes sufficiently small. In current study, $Itr_{max} = 15$.

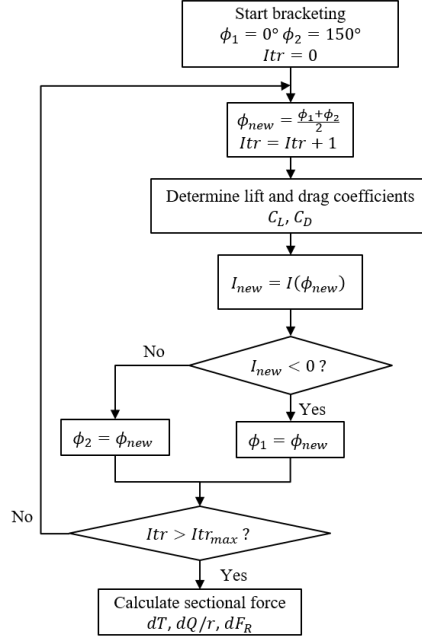


Figure 7: Flow Chart for Solving Blade Element Forces

It is worth noticing that the segmentation in momentum analysis allows for independent solution at different propeller blades, and thus it describes better the asymmetry in blade loading when subjected to non-uniform flow condition. However the assumption that flow is accelerating in well-defined annulus is difficult to justify, especially when the wake is highly skewed. In these conditions, The induced velocity distribution is solved using inflow model presented in the following section.

D. Pitt & Peters Inflow model

In 1974, Bramwell²⁰ showed that by assuming small perturbation, the Euler's equation can be linearised. This leads to two conclusions : 1. pressure distribution over the flow field satisfies Laplace equation, 2. induced velocity can be obtained in an integral form of pressure gradient. Further developing the theory, Pitt & Peters have presented a state-space dynamic inflow model which obtains bi-linear induce velocity distribution on the rotor disk plane with thrust, pitch and yaw moment. The model is well documented in various articles,^{9, 21, 22} and is subsequently expanded to include higher harmonics,^{11, 23} or to induced velocity off disk plane.²⁴ For performance analysis, the original Pitt & Peters inflow model is sufficient, and will be briefly introduced following largely the derivation by Peters and HaQuang.⁹

The induced flow distribution is described as a three-states bi-linear function over rotor disk.

$$\nu(r, \psi) = \nu_0 + \nu_s \bar{r} \sin \psi + \nu_c \bar{r} \cos \psi \quad (19)$$

where $\nu = \frac{V_A}{\Omega R}$ is the non-dimensional axial induced velocity, ν_0 , ν_s and ν_c are uniform, lateral and longitudinal variations, which are the three states defining its distribution. The induced velocity field is sketched in figure 8.

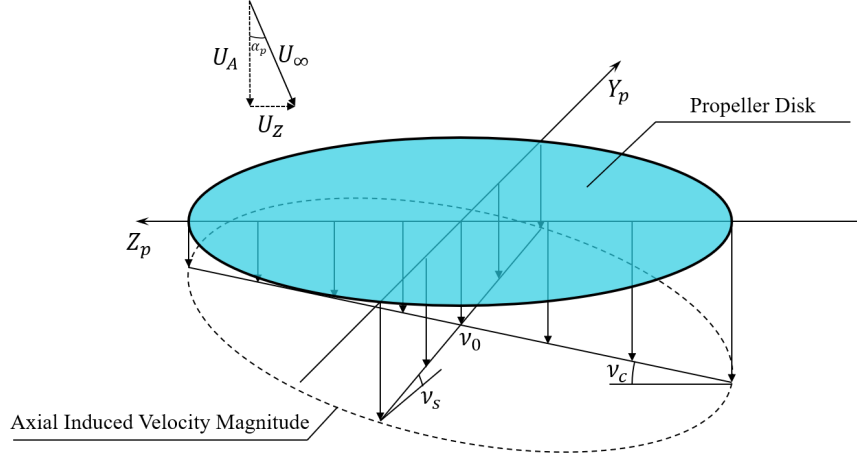


Figure 8: Bi-linear distribution of induced velocity

A state-space dynamic inflow model is obtained by solving for the pressure terms as Legendre polynomials that satisfy Laplace equation. Only first-harmonic terms are kept to give bi-linear distribution. As a result, the induced velocity states are related directly with thrust, yaw and pitch moment.

$$[M] \begin{bmatrix} \dot{\nu}_0 \\ \dot{\nu}_s \\ \dot{\nu}_c \end{bmatrix} + [\tilde{V}] [\mathcal{L}]^{-1} \begin{bmatrix} \nu_0 \\ \nu_s \\ \nu_c \end{bmatrix} = \begin{bmatrix} C_T \\ C_n \\ C_p \end{bmatrix} \quad (20)$$

where the first term on the left-hand side is the apparent mass term that represents wake transient, and is ignored since only steady wake state is desired in current study. The second term is non-linear inflow gain matrix. $[\tilde{V}]$ is mass-flow parameter matrix which gives weighted downstream velocities for thrust, pitch and yaw moments.

$$\tilde{V} = \begin{bmatrix} \lambda_T & 0 & 0 \\ 0 & \lambda & 0 \\ 0 & 0 & \lambda \end{bmatrix} \quad (21)$$

where $\lambda_T = \frac{\sqrt{(U_A + V_{A_m})^2 + U_Z^2}}{\Omega R}$ is the total inflow ratio. V_{A_m} is the disk-averaged axial induced velocity obtained from momentum theory. λ is the mass-flow parameter that considers cyclic disturbances, and is given by $\lambda = \frac{U_Z^2 + (2V_{A_m} - U_A)(V_{A_m} - U_A)}{\sqrt{(U_A + V_{A_m})^2 + U_Z^2}}$.

Matrix $[\mathcal{L}]$ contains the influence from skewed wake. The terms in gain matrix are functions of the wake skew angle $\chi = \tan^{-1} \frac{U_A + V_{A_m}}{U_Z}$, depicted in figure 9.

The gain matrix $[\mathcal{L}]$ is given below.⁹

$$\mathcal{L} = \begin{bmatrix} \frac{1}{2} & 0 & -\frac{15\pi}{64} \sqrt{\frac{1 - \sin \chi}{1 + \sin \chi}} \frac{1}{hi} \\ 0 & \frac{4}{1 + \sin \chi} & 0 \\ \frac{15\pi}{64} \sqrt{\frac{1 - \sin \chi}{1 + \sin \chi}} & 0 & \frac{4 \sin \chi}{1 + \sin \chi} \end{bmatrix} \quad (22)$$

To solve the non-linear system, an iterative method is used. Induced velocity field is initialised with a BEMT solution in axial condition, using U_A as the axial velocity. Thrust, pitch and yaw moments are then obtained by BET taking U_Z into consideration. The non-dimensional coefficients are then fed in the state-space model 20 to update state variable ν_0 , ν_s and ν_c . The new values are compared with the previous iteration until the maximum difference reduces below a threshold.

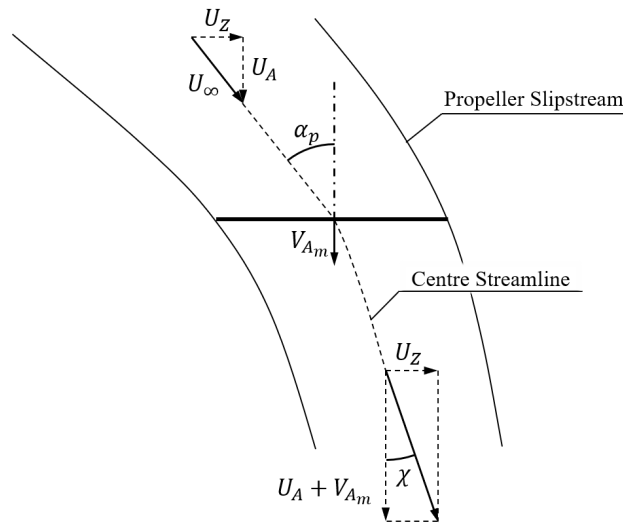


Figure 9: Wake Skew Angle

E. Blade Sectional Force

This section presents two sub-models to correct for 3D effects on blade section aerodynamics specific to high incidence condition. The methods mentioned previously calculates blade loading using BET, and thus 2D aerofoil polar is used to compute sectional loads.

However the presence of radial flow component has proven important to estimate rotor performance at high incidence angle.¹⁸

Local radial flow induced by the centrifugal force from rotation acts to delay stall onset compared to translating 2D airfoil, and failure to include such effect results in under-prediction of thrust at low advance ratio^{25, 26} or high incidence angle.⁷ The rotational stall delay model is described in the first part of this section.

The free stream component projected in the blade radial direction creates additional drag that contributes to propeller normal force N . This effect is well studied in helicopter literature to estimate profile power during forward flight.^{18, 19} The correction is presented in the second part of this section, and generally follows the analysis by Johnson.¹⁸

1. Rotational stall delay

The delayed stall at the inner sections of propeller blade is first documented by Himmelskamp²⁵ during experiment. While working in axial flow condition, the problem is most prominent when the advance ratio is small. For propeller at high incidence angle, the axial component of free stream velocity is reduced, and thus the propeller performance largely resembles those at lower advance ratio. It is for this reason that rotational stall delay is important for the current study.

Snel et al²⁷ studied this problem by performing an order-of-magnitude analysis on boundary layer equations in rotating frame. The study revealed that tip-wise flow component acts as a favourable pressure gradient through Coriolis' effect. Du et al²⁸ followed a similar approach and solved the equations for the trailing edge separation point by assuming a linear edge velocity distribution, their finding confirmed that the trailing edge separation was indeed delayed. Various studies on flapping wings²⁹ and rotary wings³⁰ also suggest that the mass transportation of tip-wise radial flow provides a stabilization mechanism for leading edge vortex, which enhances lift generation. Unfortunately studies on rotational stall delay effect for propeller at high incidence angle is scarce.

Following the analysis by Snel et al, different models were proposed. Breton et al³¹ compared 6 of them against wind tunnel data from NREL's phase VI experiment. The result suggested that Snel's model provides a good balance between complexity and accuracy, and is suitable for implementation in a BET program. Therefore the current study adopts Snel's model for axial wind tunnel analysis.

Snel's model corrects aerofoil lift and drag coefficients for rotational effects using the following formulae:

$$C_{L,3D} = C_{L,2D} + f_L \Delta C_L \quad (23)$$

$$C_{D,3D} = C_{D,2D} + f_D \Delta C_D \quad (24)$$

where $C_{L,3D}$ and $C_{D,3D}$ are the corrected lift and drag coefficient; $C_{L,2D}$ and $C_{D,2D}$ are the unaltered lift and drag coefficient obtained from 2D polar. $\Delta C_L = C_{L\alpha} (\alpha - \alpha_0) - C_{L,2D}$ and $\Delta C_D = C_{D,2D} - C_{D_0}$, which are the differences in lift and drag coefficients if the flow had not separated. Therefore Snel's correction is a weighted average between ideal linear lift and the viscous effect.

The original weighting function proposed by Snel are:

$$\begin{aligned} f_L &= \tanh 3 (c/r)^2 \\ f_D &= 0 \end{aligned}$$

where the ratio c/r is the reciprocal of Rossby number Ro for a rotating flow field, such as propeller or helicopter rotor.²⁹

Although the original Snel's model appeared to provide reasonable corrections, further modifications were suggested for better agreement with experimental observations in Breton et al:³¹ 1. the model should be switched off for blade section situated outside of 80% radius; 2. a fading model is added so that the effect reduces linearly to zero at 50° angle of attack.

Application of this model results in under-prediction of propeller torque and yaw moment. To correct the torque estimation, an increase in drag coefficient is added. This modification during rotational stall delay was suggested by Breton et al. The correction functions used in the current study are given below.

$$\begin{aligned} f_L &= \tanh 3 (c/r)^2 \\ f_D &= f_L/2 \end{aligned}$$

The underestimation of yaw moment is attributed to the absence of non-uniform flow condition in Rossby number calculation, as previous studies all focused on propeller working in axial flow condition. A further study on the scaling of Navier-Stokes equation in a rotating flow field suggests that Rossby number should be generalized to include variation on local flow condition.

$$Ro = \frac{1}{1 + J^2} \frac{r}{c} \quad (25)$$

where $J^\phi = \frac{2\pi U_A}{\Omega D + 2\pi U_T}$ is the local advance ratio, which includes the influence of in-plane free stream component.

2. Free stream radial flow correction

In section B, the blade analysis ignores radial flow component from free stream flow. The effect is usually negligible for thrust and torque analysis, but not true for normal force N .¹⁸ As the propeller blade aligns with free stream direction, the viscous drag created by this radial component makes contribution to normal force that is not negligible. This effect is usually modelled in helicopter rotor analysis by drawing an analogy with swept wing. This correction can be easily integrated with BET with 2D polar.

Consider the top view of blade section in figure 10, the tangential velocity W_T is perpendicular to the leading edge, while the radial component W_R points toward the blade root. Airflow thus meets the leading edge at a yaw angle $\Lambda = \tan^{-1} \frac{W_R}{W_T}$. The aerofoil profile can be taken in two different sections: 1. the unyawed blade section (I); 2. the yawed blade section (II). To include the influence of free stream radial component, the yawed blade section (II) should be considered, sectional lift and drag force can be obtained using flow condition in the yawed section. Thrust, tangential force as well as radial force can be converted from these lift and drag in the following manner.

$$dT = dL_y \cos \phi_y - dD_y \sin \phi_y \quad (26)$$

$$dQ/r = (dL_y \sin \phi_y + dD_y \cos \phi_y) \cos \Lambda \quad (27)$$

$$dF_R = (dL_y \sin \phi_y + dD_y \cos \phi_y) \sin \Lambda = \tan \Lambda dQ/r \quad (28)$$

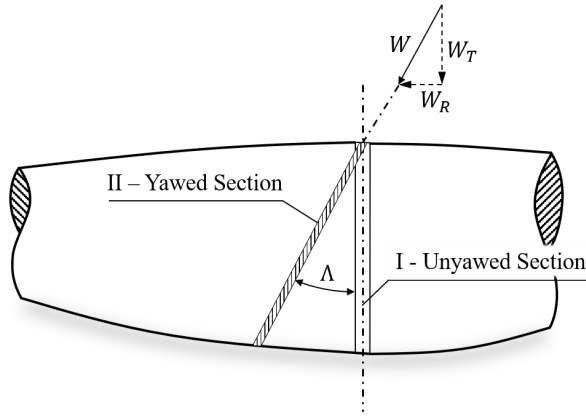


Figure 10: Top View of Blade Section with Radial Free Stream Component

where subscript $_y$ denotes quantities in the yawed section.

The yawed section profile, however, is usually not known and difficult to determine. Therefore the sectional lift and drag coefficients are usually determined through the unyawed section profile (I), and converted into forces in the yawed section by some assumptions.

The first assumption states that lift remains the same in yawed and unyawed section. Indeed for incompressible, 2D dominant flow, the blade subjected to a radial velocity should produce the same amount of lift when there isn't a radial flow but the observer is moving along the radial direction with the same velocity. Therefore

$$dL_y = dL = \frac{1}{2} \rho W^2 c C_L(\alpha) dr \quad (29)$$

Secondly, the yaw angle is assumed to be small, and therefore the drag polar can be approximated by the drag polar of unyawed section.

$$C_{D_y}(\alpha) = C_D(\alpha) \quad (30)$$

During calculation, the angle of attack in yawed section α_y should be applied along with respective wind velocity W_y , chord length c_y and differential radius dr_y .

The yawed angle of attack is related to that of unyawed section by the following relationship.

$$\alpha_y = \alpha \cos \Lambda \quad (31)$$

And thus the drag force can be obtained.

$$\begin{aligned} dD_y &= \frac{1}{2} \rho W_y^2 c_y C_{D_y}(\alpha_y) dr_y \\ &= \frac{1}{2} \rho W_y^2 c C_D(\alpha_y) dr \end{aligned} \quad (32)$$

where $W_y^2 = W_A^2 + W_T^2 + W_R^2$, and the elongation of chord length c_y is canceled by the reduction in differential radius dr_y .

Thus the sectional thrust, tangential and radial forces can be obtained through equations 31, 29, 32, and 26 - 28.

III. Results

To validate the reduced-order model, non-dimensional coefficients are obtained from calculation with an azimuthal incremental step-size of 1° . The reduced-order model switches from BEM method to Pitt & Peters inflow model at advance ratio $J = 0.3$. The values are presented in non-dimensional forms as thrust, power, normal force and yaw moment coefficients, defined respectively below.

$$\begin{aligned}
C_T &= \frac{T}{\rho (\Omega/2\pi)^2 D^4} & C_N &= \frac{N}{\rho (\Omega/2\pi)^2 D^4} \\
C_P &= \frac{P}{\rho (\Omega/2\pi)^3 D^5} & C_n &= \frac{n}{\rho (\Omega/2\pi)^2 D^5}
\end{aligned} \tag{33}$$

where P is mechanical power to sustain propeller rotation against aerodynamic torque $P = Q\Omega$.

The results are compared to an experiment conducted by Yaggy et al¹⁴ in NASA Ames 40- by 80-foot wind tunnel. General characteristics of the full-scale propeller are presented in table 1. The set-up allowed incidence angle to change from 0° to 85° .

Propeller	Curtiss C6348-C500
Diameter	12 feet (3.66 m)
Number of blades	3
Airfoil sections	NACA 16 series
Propeller pitch angle at 0.75R	35°

Table 1: Physical characteristics of testing propeller

To further validate the engineering method, a CFD calculation is presented for the same propeller operating at advance ratios up to 1.0. The effect of incidence angle is simulated by gliding mesh technique and the flow field is analysed by solving URANS equations. Detailed set-up of the calculation can be found in the appendix.

A. Overall Comparison

The results are presented for two incidence angles, $\alpha_p = 0^\circ$ and 45° . The data for each incidence angle are plotted against various effective advance ratio calculated from free stream axial component $J' = \pi \frac{U_A}{\Omega R} = \pi \frac{U_\infty \cos \alpha}{\Omega R}$.

1. Propeller at incidence angle $\alpha_p = 0^\circ$ (axial flow)

The axial case is used to validate the engineering method and URANS. In figure 11, thrust coefficient is plotted in solid line, and power coefficient is in dash line.

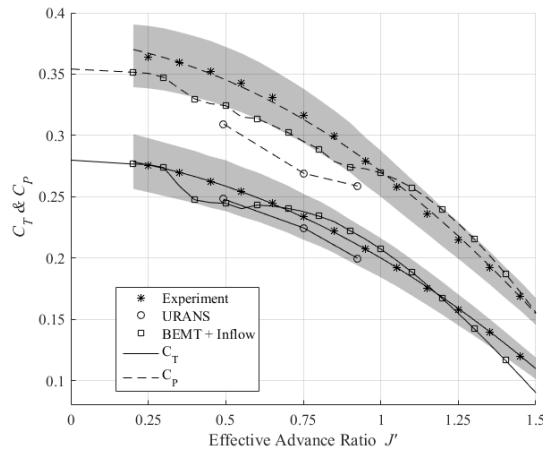


Figure 11: Thrust and Power Coefficients at $\alpha_p = 0^\circ$

Asterisks mark the experimental data found in Yaggy et al.¹⁴ Both thrust and power coefficients show a non-linear reduction as advance ratio increases. From the velocity diagram 4, the axial free stream component acts to decrease blade angle of attack, hence the reduction in lift and drag coefficients at high speed.

The results from reduced-order model and URANS calculation are presented and marked respectively by square and circle markers. Both methods correctly predicts the reduction in thrust and power coefficients. The gray area represents error estimated in Yaggy et al.¹⁴ The reduced-order model prediction lie closely within the tolerance. At small advance ratio, there appears to be a noticeable dip in thrust and power coefficients. This is explained by the premature stall at certain blade sections, and suggests further improvements on stall delay prediction.

The thrust calculation from URANS agrees with experimental data well, however the power coefficients are underestimated. This suggests that the viscous effects computed from RANS model may be different from the flow condition on the propeller blade. This causes discrepancies in drag predictions resulting in lower power consumption than measured.

2. Propeller at incidence angle $\alpha_p = 45^\circ$

The results at 45° incidence angle are plotted in the same fashion in figure 12. Compared to the experimental measurement in figure 11, thrust and coefficients at the lowest advance ratio $J' = 0.2$ remain almost the same, since the influence of free stream is small compared to rotational speed.

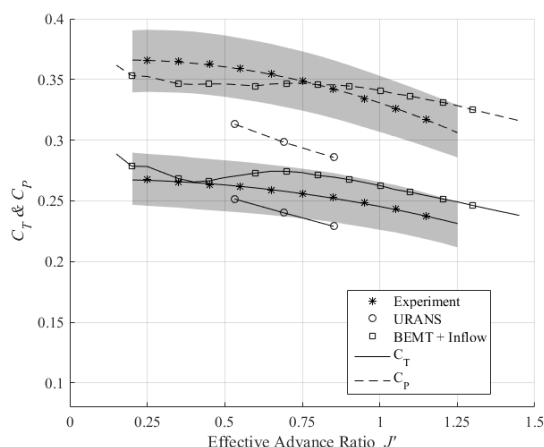


Figure 12: Thrust and Power Coefficients at $\alpha_p = 45^\circ$

As advance ratio increases, the coefficients decrease but to is much more gentle compared to axial case. The thrust coefficient at $J' = 1.25$ is about 1.4 times to its value at axial condition. This trend can be explained by advancing-retreating blade effect. At the advancing side, the tangential component from free stream increases both relative wind speed W and effective angle of attack α . The opposite is true for retreating blade, but as the dynamic pressure scales with the square of relative wind speed, the effect is more prominent for advancing blade. Therefore, the net effect on the rotor disk is an increase of thrust and torque.

Both numerical models gives a more gentle reduction compared to the results in figure 11. The reduced-order model captures this variation well with a gradual decrease consistent with experimental data. The premature stall is still noticeable, but to a lesser degree.

The URANS calculation however, gives a steeper reduction in thrust, but still within tolerance. Power coefficient is again underestimated. The degradation in URANS calculation is attributed to increased separation region at higher incidence angle. This may indicate that, although suitable for design point analysis, RANS model still needs more adjustments to accurately capture flow features specific to propeller operating at high incidence.

Non-axisymmetric forces and moments are also plotted for $\alpha_p = 45^\circ$ in figure 13. Three curves are given with solid line representing normal force coefficient C_N , dash line for pitch moment coefficient C_p and dotted line for yaw moment coefficient C_n .

Normal force coefficient exhibits a quasi-linear trend. Following the notion in figure 2, the force increases in the downstream direction on rotor disk plane. This is because advancing blades produce larger tangential force pointing towards downstream direction than that from retreating blades. The net effect between two

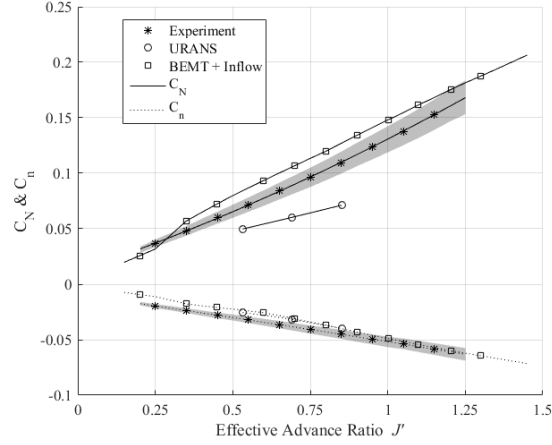


Figure 13: Normal Force, Pitch Moment and Yaw Moment Coefficients at $\alpha_p = 45^\circ$

sides of rotor disk is a force component directing downstream. As advance ratio increases, this asymmetric effect intensifies and renders the quasi-linear trend in normal force coefficient C_N .

The reduced-order model gives slightly higher values than the measurements, for most advance ratios, the curve is displaced by a constant value of 0.01 from experimental data. The force gradient is in good agreement. Results from URANS gives smaller value, which is consistent with the underestimation in power coefficient. Since the normal force is more closely related to drag produced on the blades, a reduction in power should result in a similar under prediction in normal force. The force gradient also appears shallower than the other two sets of data.

Yaw moment coefficient C_n also increases quasi-linearly with advance ratio, and the moment rotates always about negative Z_p axis, from advancing side towards retreating side according to figure 2. At high incidence angle, as discussed before, additional thrust is concentrated by advancing blades, and thus thrust centre shifts from propeller hub to advancing side. The shift of thrust centre creates yaw moment.

The two numerical models all give consistent prediction on yaw moment as shown by the close relation of three curves. This can be partly explained by the favourable trend in thrust calculation, since yaw moment is more closely associated with thrust generation. In addition, the moment also depends on thrust distribution over rotor disk, and thus supports the calculation methods on non-uniform loading propeller.

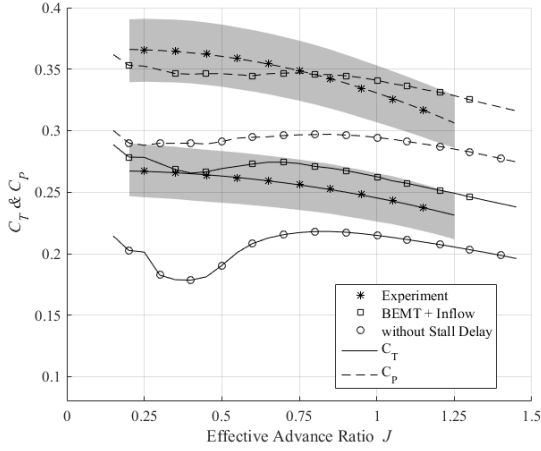
B. Effect of Stall Delay

The stall delay model is introduced to compensate the rotational effect that delays stall onset on blade sections at lower advance ratio. Its effect on thrust and power coefficients can be seen in figure 14a.

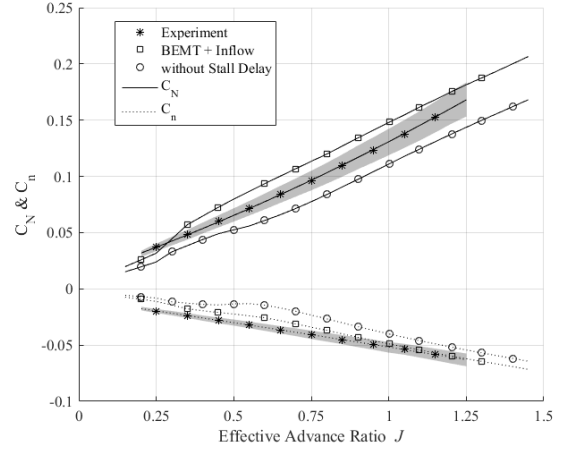
In the figure, an additional curve marked by circle symbol is added to the experimental data and the previous calculation from reduced-order model. It can be seen that at 45° , the rotational effect is great. At high advance ratio, the curves without stall delay fall below the previous calculation while exhibiting a similar gentle reduction in thrust and power coefficients. When the advance ratio decreases, the thrust curve neglecting stall delay effect lowers sharply at advance ratio around 0.6, showing a distinctive sign of blade stall. The thrust and power coefficient thus falls well below experimental data, while the prediction including stall delay effect is able to follow the measurement down to $J' = 0.2$.

The stall delay also affects normal force and yaw moment calculation, as shown in figure 14b.

Without stall delay effect, the normal force and yaw moment are underestimated. The affected normal force coefficient is still quasi-linear, but at a lower value. The impact of stall delay effect is more prominent in yaw moment calculation such that the curve is no longer quasi-linear at low advance ratio. As a consequence of thrust reduction, yaw moment calculated at advance ratio lower than $J' = 0.6$ is much weaker, and thus the trend is non-linear at low speed regime. At advance ration $J' = 0.5$, the yaw moment coefficient is about half of the experimental data, and thus showing the necessity in including stall delay correction.



(a) Thrust and Power Coefficients



(b) Normal Force and Yaw Moment Coefficients

Figure 14: Stall Delay Effect on Propeller Performance at $\alpha_p = 45^\circ$

C. Effect of Radial Flow Correction

The radial flow correction calculates blade sectional load in the yawed section by considering all three components of free stream flow. The additional blade span-wise drag computed in this method contributes to normal force. This effect is discussed in this section and shown in figure 15.

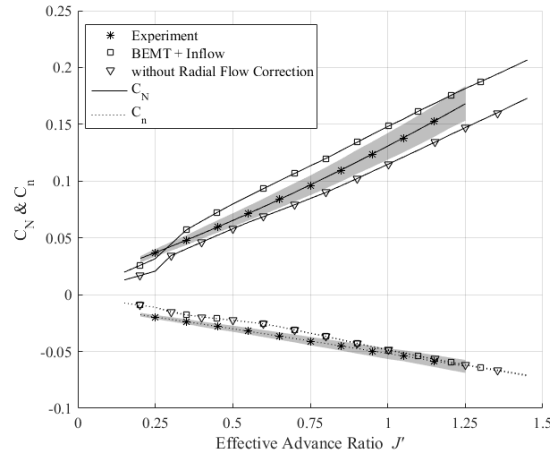


Figure 15: Radial Flow Correction on Normal Force Coefficient at $\alpha_p = 45^\circ$

In the plot, an additional curve calculated without radial flow correction is marked by circle symbol, and compared against normal force and yaw moment coefficient from experimental data and normal calculation. This curve still increases quasi-linearly with advance ratio, but shows an underestimation of normal force for the plotted advance ratio range. At 45° , this correction is already noticeable, and its effect is expected to increase at higher incidence angle. The difference shows a normal force contribution due to the span-wise drag is required for propeller performance at high incidence.

Unlike in figure 14b, only normal force coefficient is underestimated when radial flow correction is disabled, and yaw moment coefficient is unaffected. This is expected since the correction mainly adds span-wise drag in normal force calculation, sectional lift and drag characteristics are not significantly altered.

IV. Conclusion

The current study presented an effective reduced-order model to estimate propeller forces and moments at an incidence angle ranging from 0° to 90° as typical during VTOL transition flight. The model was focused on rapid preliminary design, and is based on BEM theory and Pitt & Peters inflow model. To fully simulate the influence of non-axisymmetric flow condition, stall delay effect and radial flow corrections were added.

Results were compared with similar experiment and URANS calculation. It was found that the thrust and power fall-off at high advance ratio is reduced at high incidence angle, and a quasi-linear increase with advance ratio in normal force and yaw moment should be expected. These propeller behaviours could give valuable insights in the study of VTOL transition flight.

Compared with both experimental data and URANS calculations, the reduced-order model has computed very consistent results in both axial flight and high incidence conditions. Contrasting with URANS calculation, the method can capture important global variations in propeller thrust, power, normal force and yaw moment at a greatly reduced computational cost. This was further confirmed by studying the effects of additional sub-models individually, which showed improvements of prediction when each sub-model had been included. The model could be further improved by including more harmonics and radial functions in Pitt & Peters inflow model to allow more detailed induced velocity estimation, although its current state with only first-harmonics was already sufficient for preliminary performance analysis.

References

- ¹Bronz, M. and Drouin, A., "Preliminary Design Estimation of the V/STOL Airplane Performance," *International Journal of Micro Air Vehicles*, Vol. 7, No. 4, 2015, pp. 449–462.
- ²USAF, "Osprey firing flares," https://upload.wikimedia.org/wikipedia/commons/thumb/3/34/0sprey_firing_flares.jpg/1200px-0sprey_firing_flares.jpg, 2004, Online; Accessed 1 May 2018.
- ³Phillips, W. F., *Mechanics of flight*, John Wiley & Sons, 2004.
- ⁴Ribner, H. S., "Propellers in yaw," Tech. Rep. NACA-TR-820, National Advisory Committee for Aeronautics. Langley Aeronautical Lab., Langley Field, VA, United States, January 1943.
- ⁵De Young, J., "Propeller at high incidence," *Journal of Aircraft*, Vol. 2, No. 3, 1965, pp. 241–250.
- ⁶Crigler, J. L. and Gilman Jr, J., "Calculation of aerodynamic forces on a propeller in pitch or yaw," Tech. Rep. NACA-TN-2585, National Advisory Committee for Aeronautics, Langley Aeronautical Lab, Langley Field, VA, United States, 1952.
- ⁷Smith, H. R., *Engineering models of aircraft propellers at incidence*, Ph.D. thesis, University of Glasgow, 2015.
- ⁸Bramwell, A. R., Balmford, D., and Done, G., *Bramwell's helicopter dynamics*, Elsevier, 2001.
- ⁹Peters, D. A. and HaQuang, N., "Dynamic inflow for practical applications," *Journal of American Helicopter Society*, Vol. 33, October 1988, pp. 64 – 68.
- ¹⁰Peters, D. A., Boyd, D. D., and He, C. J., "Finite-State Induced-Flow Model for Rotors in Hover and Forward Flight," *Journal of the American Helicopter Society*, Vol. 34, No. 4, October 1989, pp. 5–17.
- ¹¹Peters, D. A. and He, C. J., "Finite state induced flow models. II-Three-dimensional rotor disk," *Journal of Aircraft*, Vol. 32, No. 2, March 1995, pp. 323–333.
- ¹²Benoit, B., Dequin, A.-M., Kampa, K., Grünhagen, W. V., Basset, P.-M., and Gimonet, B., "HOST, a General Helicopter Simulation Tool for Germany and France," American Helicopter Society 56th Annual Forum, Virginia Beach, VA, United States, May 2000.
- ¹³Suzuki, A., *Application of dynamic inflow theory to wind turbine rotors*, Ph.D. thesis, The University of Utah, October 2000.
- ¹⁴Yaggy, P. F. and Rogallo, V. L., "A wind-tunnel investigation of three propellers through an angle-of-attack range from 0 deg to 85 deg," Tech. Rep. NACA-TN-D-318, NASA Ames Research Center, Moffett Field, CA, United States, May 1960.
- ¹⁵Winarto, H., "BEMT Algorithm for the Prediction of the Performance of Arbitrary Propellers," *Melbourne: The Sir Lawrence Wackett Centre for Aerospace Design Technology, Royal Melbourne Institute of Technology*, 2004.
- ¹⁶Ning, S. A., "A simple solution method for the blade element momentum equations with guaranteed convergence," *Wind Energy*, Vol. 17, No. 9, 2014, pp. 1327–1345.
- ¹⁷Bianchini, A., Balduzzi, F., Rainbird, J. M., Peiro, J., Graham, J. M. R., Ferrara, G., and Ferrari, L., "An Experimental and Numerical Assessment of Airfoil Polars for Use in Darrieus Wind Turbines—Part II: Post-stall Data Extrapolation Methods," *Journal of Engineering for Gas Turbines and Power*, Vol. 138, No. 3, 2016, pp. 032603.
- ¹⁸Johnson, W., *Helicopter theory*, Courier Corporation, 2012.
- ¹⁹Leishman, G. J., *Principles of helicopter aerodynamics with CD extra*, Cambridge university press, 2006.
- ²⁰Bramwell, A., "Some Remarks on the Induced Velocity Field of a Lifting Rotor and on Glauert's Formula," *Current Papers 1301*, Aeronautical Research Council, 1974.
- ²¹Pitt, D. M. and Peters, D. A., "Theoretical prediction of dynamic-inflow derivatives," 6th European Rotorcraft and Power Lift Aircraft Forum, Bristol, England, September 1980.
- ²²Peters, D. A., "The importance of steady and dynamic inflow on the stability of rotor-body systems," NASA, Ames Research Center, Integrated Technology Rotor Methodology Assessment Workshop, Washington University, Department of Mechanical Engineering, Saint Louis, MO, United States, June 1988, pp. 181–201.
- ²³He, C., *Development and application of a generalized dynamic wake theory for lifting rotors*, Ph.D. thesis, Georgia Institute of Technology, 1989.

²⁴Morillo, J. A., *A fully three-dimensional unsteady rotor inflow model from a Galerkin approach*, Ph.D. thesis, Washington University, December 2003.

²⁵Himmelskamp, H., *Profile investigations on a rotating airscrew*, MAP, 1947.

²⁶Gur, O. and Rosen, A., “Propeller performance at low advance ratio,” *Journal of aircraft*, Vol. 42, No. 2, 2005, pp. 435–441.

²⁷Snel, H., Houwink, R., Bosschers, J., et al., *Sectional prediction of lift coefficients on rotating wind turbine blades in stall*, Netherlands Energy Research Foundation Petten, Netherlands, 1994.

²⁸Du, Z. and Selig, M. S., “A 3-D stall-delay model for horizontal axis wind turbine performance prediction,” *AIAA paper*, Vol. 21, 1998, pp. 9–19.

²⁹Lentink, D. and Dickinson, M. H., “Biofluiddynamic scaling of flapping, spinning and translating fins and wings,” *Journal of Experimental Biology*, Vol. 212, No. 16, 2009, pp. 2691–2704.

³⁰Jardin, T. and David, L., “Coriolis effects enhance lift on revolving wings,” *Physical Review E*, Vol. 91, No. 3, 2015, pp. 1–4.

³¹Breton, S.-P., Coton, F. N., and Moe, G., “A study on rotational effects and different stall delay models using a prescribed wake vortex scheme and NREL phase VI experiment data,” *Wind Energy*, Vol. 11, No. 5, 2008, pp. 459–482.

Appendix

The three-dimensional Unsteady Reynolds-Averaged Navier-Stokes equations (URANS) are numerically solved under their incompressible form using StarCCM+ commercial code. A sliding mesh approach is used where the rotor is enclosed within a spherical domain (with radius equal to 2 rotor radii) that can be tilted at an angle of attack α with respect to the free stream velocity and that can rotate at a given rotation speed within a stationary, cylindrical domain (with radius and length equal to 10 and 50 rotor radii, respectively) - see figure 16. The unstructured mesh consists of 10 million hexahedral cells, with approximately 100 cells per blade chord. The boundary conditions upstream and downstream of the rotor are implemented as velocity and pressure Dirichlet conditions, respectively. The periphery of cylindrical domain is defined using a slip-wall condition and the blades are modelled as non-slip surfaces. Time marching is achieved with a time step corresponding to $1/360^{th}$ of the rotor rotation period. Both spatial and temporal discretisations are achieved using second-order schemes. Finally, the Spalart-Allmaras model is employed for URANS turbulence closure with maximum y^+ values on the order of 1.

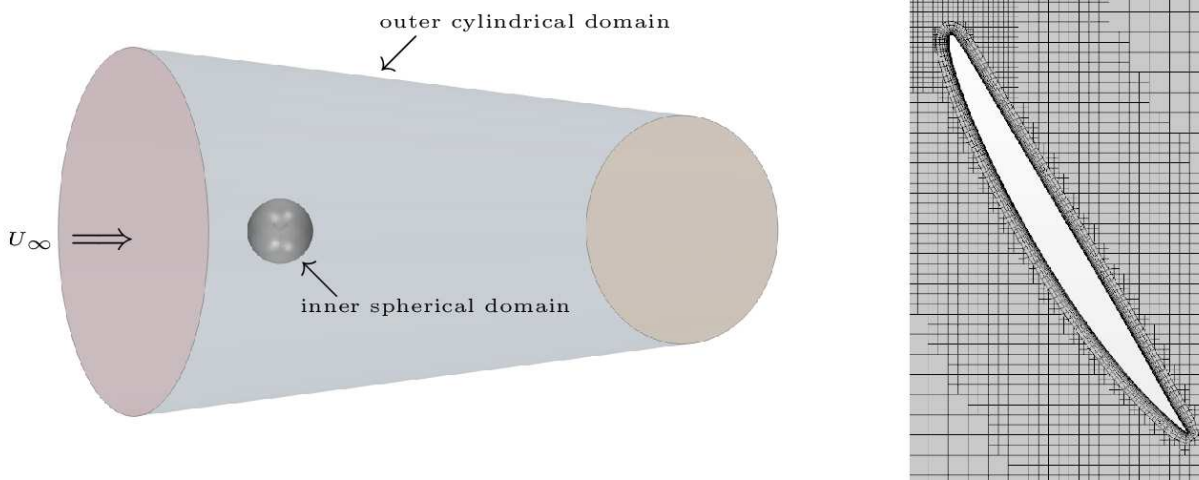


Figure 16: Computational domain (left) and close-up view of the mesh near blade section (right).

Mean aerodynamic forces and moments are obtained by averaging instantaneous signals over one rotation period after initial transients have sufficiently decayed (which requires at least five rotations of the rotor). Additional tests for a rotor operating in axial flight condition with advance ratio close to 1 showed that increasing the spatial resolution by a factor of two (approximately 200 cells per chord) resulted in changes less than 0.5% and 1% on thrust and torque, respectively.

Simulations were run on HP Xeon E5-2670 v3 processors with a typical computational cost of approximately 300 CPU hours per rotor rotation (parallel on 72 processors).